A Compact-Design Oriented Shipboard Power Supply System With Transformer Integrated Filtering Method

Qianyi Liu, *Member, IEEE*, Fang Liu, *Member, IEEE*, Runmin Zou, Shaoyang Wang, *Student Member, IEEE*, Ye Tian, Yun Wang, Liang Yuan, and Yong Li, *Senior Member, IEEE*

***Abstract*—The rapid development of modern vessel leads to higher demands on the optimization and integration of shipboard power supply system (SPSS). In this article, a compact-design oriented 12-pulse parallel operating transformer employing shared integrated filter is presented for power quality improvement of SPSS with reduced installation space. The proposed SPSS is featured with harmonic-free power supply and high integration of power equipment. The system topology is introduced first, and the distinctive compensation principle is then analyzed. Taking into account both of the winding impedance matching and transformer size optimization, minimum radial dimension is searched and determined in the interval of approximative zero-impedance. Moreover, the inductance calculation method of integrated reactor together with its design domain is further given out. At last, the prototype of the proposed SPSS is tested in laboratory. The experimental results verify the feasibility and effectiveness of the proposal.**

***Index Terms*—Integrated reactor, power quality, shipboard power supply system (SPSS), zero-impedance design.**

I. Introduction

INTEGRATION, modularization, and systematization are the design concept for the future all-electric shipboard power system [1]–[3]. Compared with traditional shipboard supply system, all-electric shipboard has the advantages of optimization of equipment configuration, improvement of space utilization, enhancement of shipboard stability, and improvement of shipboard crypticity. Due to the deprecation of rotary converter set, the power electronic converter becomes the core of increasing electrical equipment, such as variable-frequency drives, and efficient lighting and radar [4].

Harmonic performance is an essential requirement of power electronic based all-electric shipboard power system [5], [6]. The IEEE recommended practice of shipboard design indicates that harmonic distortion is possible to cause overheating of other elements in the distribution system and improper operation of power devices [7]. Taking propulsion transformer as an example, harmonic components can drive heat loss within the transformer. These losses include eddy currents, hysteresis, copper losses, and stray flux losses, which may cause failure due to overheating. Moreover, the potential resonance may be excited between transformer winding inductance and supply capacitance in some extreme cases. To enhance the power system robustness, additional capacity of transformer is always required when supplying nonlinear loads [8], [9].

Following methods are considered as general practice for power quality improvement of shipboard.

1) Heavy filter: Passive filter requires large installation space, which is not satisfied with the development tendency of high integration and high power-density of all-electric shipboard. Moreover, the passive filter generally adopts partial tuning design to avoid resonance risk, which inevitably results in poor filtering performance [10]–[13].
2) Multiphase rectifier with small filters: Two or more phase-shift transformers are installed to constitute multiphase rectifier. Cooperated with a small filter, harmonic elimination can be realized [14]–[16]. However, there must be tradeoffs between increased phase count (viz. increased rectifier complexity) and improved power quality.
3) Pulsewidth modulated (PWM) operation with higher switching frequency: Advanced PWM technology is able to realize satisfactory supply quality. The complicated control strategies virtually increase the realization difficulty and reliability compared with passive method [17]–[19].

Some latest scientific studies also involve the three methods. A cost-effective compensator based on fixed capacitor-thyristor controlled reactor is added to the main switchboard in parallel as an additional device in [11]. The compensator has the advantages of wide compensation range and high harmonic filtering

Manuscript received March 23, 2021; revised June 27, 2021; accepted August 2, 2021. Date of publication August 6, 2021; date of current version October 15, 2021. This work was supported in part by the International Science and Technology Cooperation Program of China under Grant 2018YFE0125300, in part by the National Natural Science Foundation of China under Grants 61973318 and 52061130217, in part by the Distinguished Young Foundation of Hunan Province of China under Grant 2020JJ2045, in part by the Innovative Construction Program of Hunan Province of China under Grant 2019RS1016, in part by the 111 Project of China under Grant B17016, in part by the Key R&D Program of Hunan Province of China under Project 2020WK2007, and in part by the Excellent Innovation Youth Program of Changsha of China under Grant KQ2009037. Recommended for publication by Associate Editor Q. Li. *(Corresponding authors: Fang Liu and Liang Yuan.)*

Qianyi Liu, Fang Liu, Runmin Zou, Yun Wang, and Liang Yuan are with the School of Automation, Central South University, Changsha 410083, China (e-mail: liu7y@foxmail.com; csuliufang@csu.edu.cn; rmzou@csu.edu.cn; wangyun19@csu.edu.cn; liang.yuan@csu.edu.cn).

Shaoyang Wang, Ye Tian, and Yong Li are with the College of Electrical and Information Engineering, Hunan University, Changsha 410082, China (e-mail: wsy0670@foxmail.com; universe0718@163.com; yongli@hnu.edu.cn).

Color versions of one or more figures in this article are available at https://doi.org/10.1109/TPEL.2021.3102938.

Digital Object Identifier 10.1109/TPEL.2021.3102938

ability. But the large volume makes it unsuitable for installation within restricted space. Kim and Lai [14] proposed a shunt Y-Δ transformer with 30° phase shift to replace the phase-shift transformer in shipboard, so that the harmonics can be trapped into the transformer and, thus, be offset, which realizes the same harmonic cancellation performance with reduced transformer size. However, it loses the function of voltage conversion and insulated isolation. Furthermore, a space vector PWM strategy is proposed to suppress the switching frequency harmonics in [17]. The fluctuation of converter current is reduced due to voltage space vector, and thus, the lifetime of dc capacitor is extended.

Designed for the residential distribution station and marine application, where the installation space of power equipment is strictly restricted, C. Liang *et al.* [20] presented a filtering reactor integrated method. By means of the inverse symmetry design on the transformer coil, the winding can be decoupled and work as an independent filtering reactor. Compared with the conventional reactor, which requires enough distance to avoid electromagnetic interference [21], the installation space of integrated reactor (IR) is considerably reduced, while the radial dimension of transformer is slightly increased. Similarly, the inductive power filtering method utilizes the transformer winding to realize harmonic elimination, but also improves the electromagnetic environment inside the transformer and enhances the operating efficiency [22]. The abovementioned filtering methods are collectively named *transformer integrated filtering method* (TIFM) in this article.

Based on TIFM, this article proposes a compact-design oriented 12-pulse parallel operating transformer with shared integrated filter for the all-electric shipboard power supply system (SPSS), with the characteristics of high integration, harmonic free, and low loss. The main tasks dealt in this article are listed as follows.

1) The filtering mechanism is revealed by means of the circuit model. The flowing path of harmonic components in the TIFM based SPSS (TIFM-SPSS) is analyzed.
2) To balance the zero-winding-impedance constraint and the overall size optimization, the minimum radial dimension of the transformer is obtained in the interval of approximative zero-impedance.
3) The inductance design method of IR is further studied. And the available inductance interval is given out.
4) The feasibility and effectiveness of TIFM-SPSS is testified by the down-scaled prototype.

This article is organized as follows. The system topology of TIFM-SPSS is introduced in Section II. In Section III, the filtering mechanism is revealed by means of circuit model. In Section IV, the compact design of the zero-impedance winding and the integrated reactor design are further illuminated. Moreover, Section V gives the experimental results. Finally, Section VI concludes this article.

II. System Topology

Fig. 1 shows the comparison of the proposed TIFM-SPSS and the conventional topology. Two pair of main generators are adopted in parallel as the power source, each pair includes

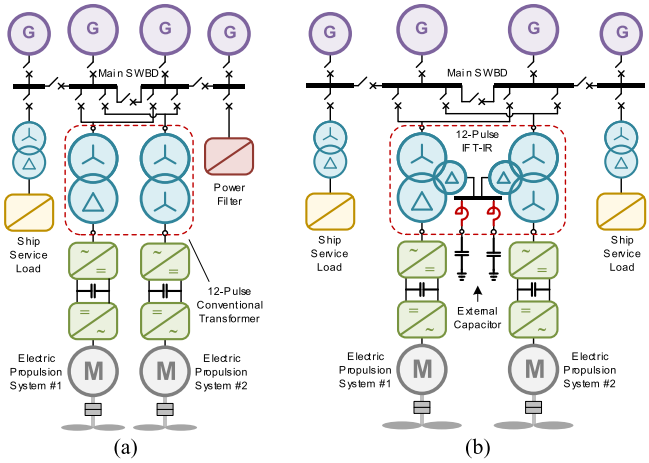

Fig. 1. Comparison between (a) traditional SPSS and (b) TIFM-SPSS.

two diesel generators with different capacity, which is beneficial to enhance the redundancy and supply reliability [23]. All the generators are connected to the main switchboard, which can be regarded as the point of common coupling, the switchboard is responsible for the power distribution of propulsion drive load and ship service load. The Y-Δ connected transformer is used for ship service load (communication load, navigation load, hotel load, etc.) with less harmonic generation. Power filter is connected to switchboard for power quality management in conventional structure [11], [12], while it is always bulky (for passive filter) or high cost (for active filter).

Compared the proposal with conventional structure, the main difference is the propulsion transformer. To constitute 12-pulse rectifier, the traditional topology uses two two-winding transformers, whose secondary windings adopt Y-connection and Δ-connection. In this way, only $12i\pm1$ ($i = 1, 2, 3\ldots$) order harmonic components exist in the current flowing into the generators. Even so, the power supply quality cannot be satisfied in some cases. The proposed structure uses two inductive filtering transformers with integrated reactor (IFT-IR) to constitute 12-pulse rectifier, as shown in Fig. 1(b). Two sets of passive filters tuned at 11th and 13th harmonic frequencies connect to the system via the common bus and filtering winding of IFT-IR. Most of the harmonics are eliminated by the common bus and passive filters, i.e., hardly any harmonics can be induced at the primary side of the transformer.

As the model shown in Fig. 2, IFT-IR is a four-winding transformer. The primary winding (W1) is connected to the switchboard, and the load winding (W2) accesses to the rectifier. The tertiary winding (W3) is used for harmonic suppression, which adopts zero-impedance design, called filtering winding. The integrated reactor is arranged at the outermost place of iron core as the coupled winding (W4), with the aim to reduce the electromagnetic coupling with power winding. The compact design makes the total installation space of transformer and filter smaller.

In sum, the proposed TIFM-SPSS has the following dominant advantages.

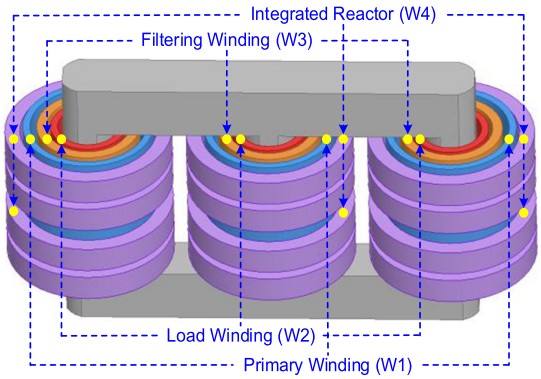

Fig. 2. Model of IFT-IR.

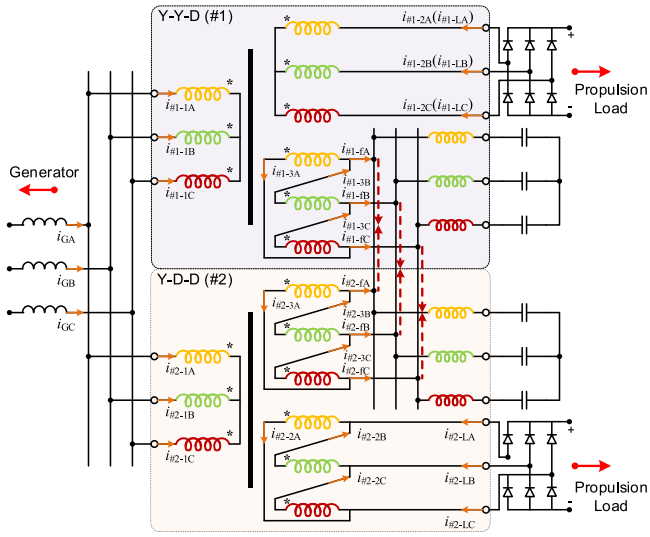

Fig. 3. Wiring scheme of the proposed IFT-IR.

1) High integration of power equipment: Thanks to the integrated reactor and the compact winding design studied in this article, the installation area is significantly reduced.
2) High power supply quality: $6i\pm1$ ($i = 1, 3, 5\ldots$) order and tuned order (11th and 13th) harmonics are suppressed by the common bus and filters, which realizes high quality of power supply.
3) Low operating loss: Due to most of the undesirable components are eliminated by the tertiary winding, the transformer efficiency can be improved.
4) High redundancy and reliability: The adoption of two sets of generators and transformers contributes to provide limited continuous power under fault condition.

III. Filtering Mechanism

According to the winding wiring shown in Fig. 3, the current in load winding of transformer #1 can be expressed as

$$\begin{aligned} i_{\#1-2A} = i_{\#1-LA} =& \frac{2\sqrt{3}}{\pi} I_d \left(\sin\omega t - \tfrac{1}{5}\sin 5\omega t - \tfrac{1}{7}\sin 7\omega t \right. \\ &+ \tfrac{1}{11}\sin 11\omega t + \tfrac{1}{13}\sin 13\omega t - \tfrac{1}{17}\sin 17\omega t \\ &\left. - \tfrac{1}{19}\sin 19\omega t + \ldots\right). \end{aligned} \tag{1}$$

Then, the current at load side of transformer #2 is

$$\begin{aligned} i_{\#2-LA} =& \tfrac{2\sqrt{3}}{\pi} I_d[\sin(\omega t + \tfrac{\pi}{6}) - \tfrac{1}{5}\sin(5\omega t + \tfrac{5\pi}{6}) \\ &- \tfrac{1}{7}\sin(7\omega t + \tfrac{7\pi}{6}) + \tfrac{1}{11}\sin(11\omega t + \tfrac{11\pi}{6}) \\ &+ \tfrac{1}{13}\sin(13\omega t + \tfrac{13\pi}{6}) - \tfrac{1}{17}\sin(17\omega t \\ &+ \tfrac{17\pi}{6}) - \tfrac{1}{19}\sin(19\omega t + \tfrac{19\pi}{6}) + \ldots]. \end{aligned} \tag{2}$$

After transform of Y→Δ, the current in load winding is obtained as

$$\begin{aligned} i_{\#2-2A} =& \tfrac{2}{\pi} I_d[\sin\omega t - \tfrac{1}{5}\sin(5\omega t + \pi) - \tfrac{1}{7}\sin(7\omega t + \pi) \\ &+ \tfrac{1}{11}\sin(11\omega t + 2\pi) + \tfrac{1}{13}\sin(13\omega t + 2\pi) \\ &- \tfrac{1}{17}\sin(17\omega t + \pi) - \tfrac{1}{19}\sin(19\omega t + \pi) + \ldots]. \end{aligned} \tag{3}$$

Considering the current relationship between load side and filtering side, the currents from two filtering windings flowing into filters can be calculated as

$$\begin{aligned} i_{\#1-fA} =& \tfrac{6}{\pi} I_d[k_1\sin(\omega t + \tfrac{\pi}{6}) - \tfrac{k_5}{5}\sin(5\omega t - \tfrac{\pi}{6}) \\ &- \tfrac{k_7}{7}\sin(7\omega t + \tfrac{\pi}{6}) + \tfrac{k_{11}}{11}\sin(11\omega t - \tfrac{\pi}{6}) \\ &+ \tfrac{k_{13}}{13}\sin(13\omega t + \tfrac{\pi}{6}) - \tfrac{k_{17}}{17}\sin(17\omega t - \tfrac{\pi}{6}) \\ &- \tfrac{k_{19}}{19}\sin(19\omega t + \tfrac{\pi}{6}) + \ldots] \end{aligned} \tag{4}$$

$$\begin{aligned} i_{\#2-fA} =& \tfrac{6}{\pi} I_d[k_1\sin(\omega t + \tfrac{\pi}{6}) + \tfrac{k_5}{5}\sin(5\omega t - \tfrac{\pi}{6}) \\ &+ \tfrac{k_7}{7}\sin(7\omega t + \tfrac{\pi}{6}) + \tfrac{k_{11}}{11}\sin(11\omega t - \tfrac{\pi}{6}) \\ &+ \tfrac{k_{13}}{13}\sin(13\omega t + \tfrac{\pi}{6}) + \tfrac{k_{17}}{17}\sin(17\omega t - \tfrac{\pi}{6}) \\ &+ \tfrac{k_{19}}{19}\sin(19\omega t + \tfrac{\pi}{6}) + \ldots] \end{aligned} \tag{5}$$

where k_n ($n = 6i\pm1$, $i = 1, 2, 3\ldots$) is current transform ratio from load side to filter side, which is defined in the Appendix.

In this way, the composite current in the filtering bus bar can be obtained as follows:

$$\begin{aligned} i_{\#1-fA}+i_{\#2-fA} =& \tfrac{12}{\pi} I_d[k_1\sin(\omega t + \tfrac{\pi}{6}) \\ &+ \tfrac{k_{11}}{11}\sin(11\omega t - \tfrac{\pi}{6}) + \tfrac{k_{13}}{13}\sin(13\omega t + \tfrac{\pi}{6}) \\ &+ \tfrac{k_{23}}{23}\sin(23\omega t - \tfrac{\pi}{6}) + \tfrac{k_{25}}{25}\sin(25\omega t \\ &+ \tfrac{\pi}{6}) + \tfrac{k_{35}}{35}\sin(35\omega t - \tfrac{\pi}{6}) + \ldots]. \end{aligned} \tag{6}$$

From the abovementioned equations, it can be found that, *all* the harmonic currents [$n = 6i\pm1$ ($i = 1, 3, 5\ldots$)] generated by the rectifier are cancelled each other out in the filtering bus bar. Due to the zero-impedance design of the IFT-IR explained in the Appendix, the tuned order harmonic currents ($n = 11$ and 13) continue to flow into the filters and then be eliminated, which means that most of the harmonics are suppressed in the filtering winding.

Finally, the generator side current is expressed as

$$\begin{aligned} i_{GA} =& \tfrac{4\sqrt{3}}{\pi} I_d(k_{G1}\sin\omega t + \tfrac{1}{23}k_{G23}\sin 23\omega t + \tfrac{1}{25}k_{G25}\sin 25\omega t \\ &+ \tfrac{1}{35}k_{G35}\sin 35\omega t + \tfrac{1}{37}k_{G37}\sin 37\omega t + \ldots) \end{aligned} \tag{7}$$

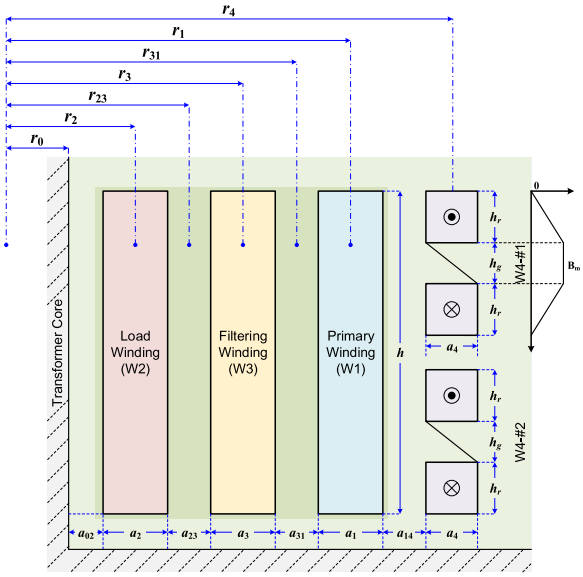

Fig. 4. Winding arrangement of IFT-IR.

where k_{Gn} is current transform ratio from load side to generator side, which is also defined in Appendix.

Obviously, by means of the parallel filtering winding and the filters, there is only fundamental current existing at generator side expect for a small amount of high order harmonics. In other word, hardly any harmonics can be induced at primary side.

IV. Transformer Design

As discussed in the previous section, the equivalent impedance of the filtering winding of the parallel operating IFTs-IR should be or approximately be zero, which puts forward quite high requirements on the winding structure design. Moreover, to reduce the installation space of the shipboard power system within restricted space, the filtering reactor has been integrated into IFT-IR, it becomes important to study how to adjust the winding distance to get the desired inductance.

This section mainly involves how to realize the zero-impedance design of filtering winding and the inductance design of IR.

A. Zero-Impedance Design

The equivalent impedance of transformer winding (Z_1, Z_2, and Z_3) can be calculated by the short-circuit impedance (Z_{k12}, Z_{k13}, and Z_{k23}) [24], i.e., $Z_3 = (Z_{k13}+Z_{k23}-Z_{k12})/2$. However, the short-circuit impedance between any two transformer windings is strongly associated with the winding dimensions. Fig. 4 gives the winding structure of IFT-IR. In the figure, r_0 is core radius; r_1, r_2, r_3, and r_4 are the center distance between core and winding; r_{23} and r_{31} are the center distance between core and air gap; a_1, a_2, a_3, and a_4 are the winding thickness; a_{02}, a_{23}, a_{31}, and a_{14} are the insulation distance between core and winding, or any two windings; h is the height of the power winding (W1, W2, and W3); h_r is the height of upper or lower subcoil; h_g is the air gap width between upper and lower subcoils.

These distances can be calculated by

$$\begin{cases} r_2 = a_{02} + \frac{a_2}{2} \\ r_{23} = a_{02} + a_2 + \frac{a_{23}}{2} \\ r_3 = a_{02} + a_2 + a_{23} + \frac{a_3}{2} \\ r_{31} = a_{02} + a_2 + a_{23} + a_3 + \frac{a_{31}}{2} \\ r_1 = a_{02} + a_2 + a_{23} + a_3 + a_{31} + \frac{a_1}{2} \\ r_4 = a_{02} + a_2 + a_{23} + a_3 + a_{31} + a_1 + a_{14} + \frac{a_4}{2}. \end{cases} \tag{8}$$

Furthermore, the short-circuit impedance between any two windings can be obtained by

$$\begin{cases} Z_{k12} = \frac{2\pi^2 f \mu_0 N_1 I_1 \rho_{12} K \sum D_{12}}{H_{12} e_t} \\ Z_{k13} = \frac{2\pi^2 f \mu_0 N_1 I_1 \rho_{13} K \sum D_{13}}{H_{13} e_t} \\ Z_{k23} = \frac{2\pi^2 f \mu_0 N_1 I_1 \rho_{23} K \sum D_{23}}{H_{23} e_t} \end{cases} \tag{9}$$

where f is the fundamental frequency; I_1 and N_1 are the rated current and turns of primary winding, respectively; μ_0 is absolute permeability, and $\mu_0 = 4\pi \times 10^{-7}$ H/m; ρ_{xy} is the Rogowski coefficient between Wx and Wy; K is additional reactance coefficient; ΣD_{xy} is the magnetic flux leakage area between Wx and Wy; e_t is the electric potential of each turn; H_{xy} is arithmetic mean height of Wx and Wy.

For the longitudinal leakage field of core structure transformer, Rogowski coefficient is calculated by

$$\begin{cases} \rho_{12} = 1 - \frac{a_2 + a_{23} + a_3 + a_{31} + a_1}{\pi H_{12}} \\ \rho_{13} = 1 - \frac{a_3 + a_{31} + a_1}{\pi H_{13}} \\ \rho_{23} = 1 - \frac{a_2 + a_{23} + a_3}{\pi H_{13}}. \end{cases} \tag{10}$$

The expression of magnetic flux leakage area used in (9) is

$$\begin{cases} \sum D_{12} = \frac{a_1 r_1}{3} + \frac{a_2 r_2}{3} + \frac{(a_{23}+a_3+a_{31})(r_2+a_2/2+r_{31}+a_{31}/2)}{2} \\ \sum D_{13} = \frac{a_1 r_1}{3} + \frac{a_3 r_3}{3} + a_{31} r_{31} \\ \sum D_{23} = \frac{a_2 r_2}{3} + \frac{a_3 r_3}{3} + a_{23} r_{23}. \end{cases} \tag{11}$$

From (8)–(11), it can be concluded that all the short-circuit impedances are interrelated to the transformer structural dimensions. After the main parameters (rated capacity, rated voltage) of the transformer are determined, the adjustment margin of winding thickness or winding height is very small. The fine-tuning of insulation distances a_{23} and a_{31} is a feasible way to realize the desired impedance. When IFT-IR satisfies the zero-impedance design, the following formula holds:

$$Z_{k13} + Z_{k23} = Z_{k12}. \tag{12}$$

According to these listed equations, Fig. 5 plots the surfaces of short-circuit impedance [Z_{k12} and $Z_{k13}+Z_{k23}$] varied with insulation distance, in which the adjustable insulation distances a_{23} and a_{31} are used as independent variable. It can be observed from Fig. 5 that, the two surfaces show an upward trend with the increase of insulation distances a_{23} and a_{31}. Due to different slope of the two surfaces, there is an intersecting line [red line] between the two surfaces. The intersecting line means the satisfaction of (12). In consequence, to realize the zero-impedance design of filtering winding, the parameter matching of the two

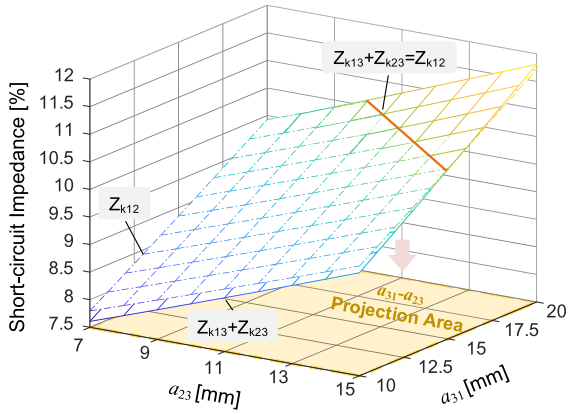

Fig. 5. Relationship between insulation distance and short-circuit impedance.

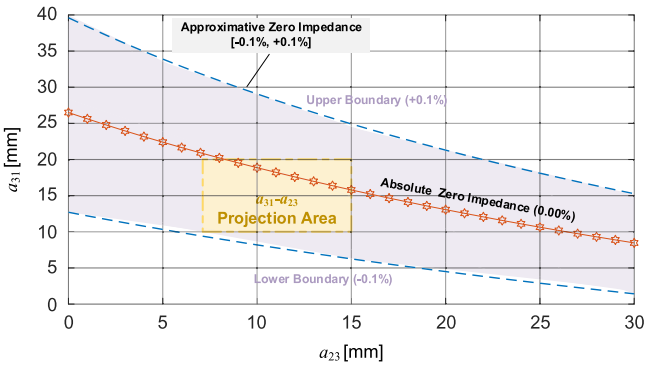

Fig. 6. Projection area of a_{31}-a_{23} and its extended plane.

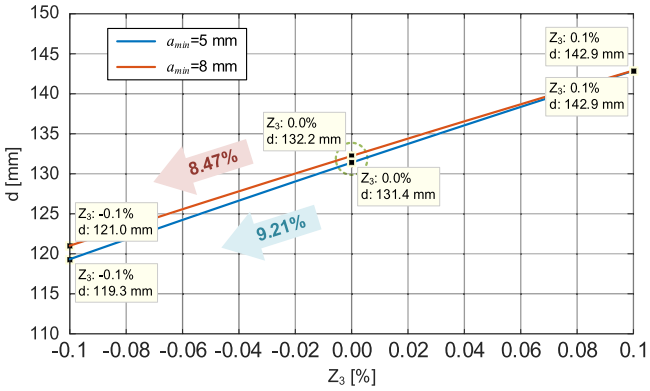

Fig. 7. Relationship between Z_3 and minimum radial dimension.

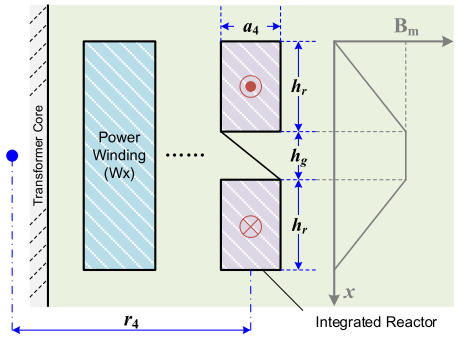

Fig. 8. Winding arrangement of integrated reactor.

insulation distances can be searched by means of the intersecting line.

Moreover, Fig. 6 shows the projection area of a_{31}-a_{23} and its extended plane. Yellow area in Fig. 6 corresponds to a_{31}-a_{23} plane in Fig. 5. The line with hexagram is just the intersecting line in Fig. 5, in which all the matched distances are one-to-one correspondence. Here, two different zero-impedance designs are defined.

1) Absolute zero-impedance: the line with hexagram, $Z_3 = 0.00\%$.
2) Approximative zero-impedance: the area bounded by lower and upper boundaries. $Z_3 \in [-0.1\%, +0.1\%]$. Assuming the filtering performance will not be influenced by the slight change of winding impedance.

To realize the application of shipboard power system within the restricted installation space, the radial dimension of the transformer winding should be as small as possible, in premise of enough insulation. Hence, it is necessary to explore in the margin area of approximative zero-impedance. The radial dimension of the transformer winding is defined as

$$d = r_0 + a_{02} + a_2 + a_{23} + a_3 + a_{31} + a_1. \tag{13}$$

Under the condition of meeting the minimum insulation distance ($a_{\min} = 5$ mm or 8 mm), we try to find the minimum radial dimension in the interval of acceptable winding impedance. Fig. 7 exhibits the results. It can be concluded that, 1) with the decrease of equivalent impedance, the corresponding minimum radial dimension is also reduced; 2) compared with the absolute zero-impedance, the minimum radial dimension can be reduced by 8.47% [$a_{\min} = 8$ mm] and 9.21% [$a_{\min} = 5$ mm], respectively, when $Z_3 = -0.1\%$.

In conclusion, the minimum radial dimension can be searched in the acceptable interval of equivalent impedance and insulation distance in the transformer design process, so that the optimization of transformer structural parameters can be realized. Furthermore, Table I lists the transformer structural parameters under different conditions.

B. Integrated Reactor Design

As the decoupling principle of IR has been thoroughly analyzed in literature [20], this section mainly discusses the inductance design of IR. Fig. 8 shows the winding arrangement of integrated reactor. Wx (x = 1, 2, or 3) is power winding, while W4 is the decoupled winding (i.e., IR) included two series-opposing connected subcoils.

In the part of upper subcoil, the maximum of magnetic field intensity and its volume are

$$\begin{cases} B_m = \frac{\mu_0 I_4 N_4 x}{h_r a_4} \\ dV = 2\pi r_4 a_4 \cdot dx. \end{cases}, x \in (0, h_r) \tag{14}$$

In the part between upper subcoil and lower subcoil, the maximum of magnetic field intensity and its volume are

$$\begin{cases} B_m = \frac{\mu_0 I_4 N_4}{a_4} \\ dV = 2\pi r_4 a_4 \cdot dx \end{cases}, x \in (h_r, h_r + h_g). \tag{15}$$

TABLE I
STRUCTURAL PARAMETERS OF IFT-IR

a_{min}	Z_3	a_{31}	a_{23}	d	Other Parameters
5 mm	+0.10%	33.9 mm	5.0 mm	142.9 mm	r_0= 50 mm; a_{20}= 8 mm; a_2= 14 mm; a_3= 18.5 mm; a_1= 13.5 mm; H_{12}= 236.15 mm; H_{13}= 226.15 mm; H_{23}= 223.70 mm; e_i= 100/45 V; K=1.
	0.00%	22.4 mm	5.0 mm	131.4 mm	
	-0.10%	10.3 mm	5.0 mm	119.3 mm	
8 mm	+0.10%	30.9 mm	8.0 mm	142.9 mm	
	0.00%	20.2 mm	8.0 mm	132.2 mm	
	-0.10%	9.0 mm	8.0 mm	121.0 mm	
Prototype	-0.04%	16.0 mm	8.0 mm	128.0 mm	

In the part of lower subcoil, the maximum of magnetic field intensity and its volume are

$$\begin{cases} B_m = \frac{\mu_0 I_4 N_4 (2h_r + h_g - x)}{h_r a_4} \\ dV = 2\pi r_4 a_4 \cdot dx \end{cases}, x \in (h_r + h_g, 2h_r + h_g). \quad (16)$$

The maximum of magnetic field energy of the two subcoils can be deduced by means of (14)–(16) as follows:

$$\begin{aligned} E_m &= \tfrac{1}{2}\int B_m H_m dV = \tfrac{1}{2\mu_0}\int B_m^2 dV \\ &= \tfrac{2\pi\mu_0 I_4^2 N_4^2}{a_4} \cdot r_4 (h_g + \tfrac{2}{3} h_r). \end{aligned} \quad (17)$$

The maximum of magnetic field energy has the following relationship with inductance:

$$E_m = I_4^2 L. \quad (18)$$

The inductance of IR can be deduced as

$$L = \frac{2\pi\mu_0 N_4^2}{a_4} \cdot r_4 \left(h_g + \frac{2}{3} h_r \right). \quad (19)$$

Rogowski correction coefficient ρ is

$$\rho = 1 - \frac{1}{\pi u}(1 - e^{-\pi u})[1 - \frac{1}{2} e^{-\pi v}(1 - e^{-\pi u})] \quad (20)$$

where u and v represent

$$\begin{cases} u = \frac{a_4}{h_g + 2h_r} \\ v = \frac{r_4 - r_0 - \frac{a_4}{2}}{h_g + 2h_r}. \end{cases} \quad (21)$$

The actual inductance after correction should be

$$L = \frac{2\pi\mu_0 N_4^2 \rho}{a_4} \cdot r_4 (h_g + \frac{2}{3} h_r). \quad (22)$$

The structural parameters that influence the inductance of IR include the height of the subcoil h_r, the insulation distance a_{14}, the air gap width between two subcoils h_g, and the winding thickness a_4. Once the rated current/voltage is determined, winding thickness, and height are hardly changed. Fig. 9(a) shows the inductance of IR varied with a_{14} and h_g. The distribution range of inductance is (0.72 mH, 0.97 mH), considering the minimum insulation distance. Similarly, the inductance is proportional to the distance parameters. Fig. 9(b) is the a_{14}-h_g projection area in Fig. 9(a). Once the minimum air gap width and inductance is determined, the insulation distance can be searched in each inductance line. According to the designed value (0.8 mH) of IR, the structural parameters are listed in Table II.

It can be learned that, because of the special structure of IR, the main flux can be offset each other [20]; the inductance of IR is generated by the leakage flux, which uses the air gap as the path. In other word, similar like air reactor, IR has the merit of excellent linearity, and is suitable for using as filtering reactor.

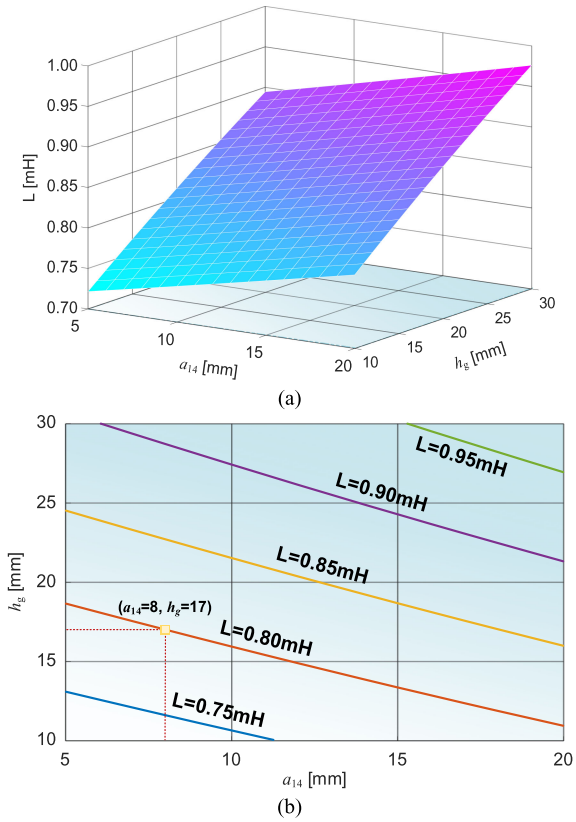

Fig. 9. Relationship between the structural parameters and the inductance. (a) Three-dimensional surface. (b) a_{14}-h_g projection area.

TABLE II
STRUCTURAL PARAMETERS OF IR

Parameter	Value	Parameter	Value
a_4 [mm]	19.5	h_r [mm]	64.6
a_{14} [mm]	8.0	h_g [mm]	17.0

V. PROTOTYPE TEST

An experimental prototype is built in the lab to test the proposed TIFM-SPSS, as shown in Fig. 10. Tables III and IV give the experimental parameters. The test results include three parts, i.e., transformer test, filtering performance test, and fundamental

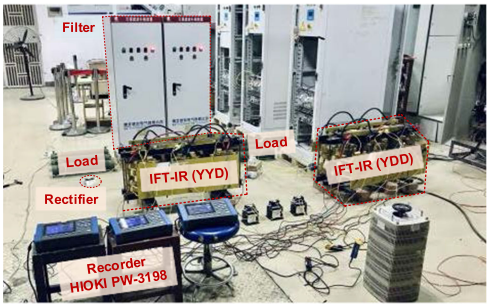

Fig. 10. Experimental platform.

TABLE III
DESIGN PARAMETERS OF IFT-IR

Serial Number	#1	#2
Winding Connection	Y-Y-D	Y-D-D
Rated Voltage [V]	400/√3, 100/√3, 100	400/√3, 100, 100
Number of Turns	104, 45, 26	104, 45, 45
Equivalent Impedance [%]	5.48, 3.76, -0.04	5.50, 3.85, -0.04
Integrated Ractor	Inductance [mH]	0.8×2
	Internal Resistance [Ω]	0.044
	Rated Current [A]	50
	Number of Turns	30 (60 for whole)

TABLE IV
DESIGN PARAMETERS OF FILTER SET

Serial Number	#1	#2
Tuned Frequency [Hz]	550	650
Compensation Capacity [Var]	110	78
Inductance-IR [mH]	0.8	0.8
Capacitance [μF]	104.67	74.94

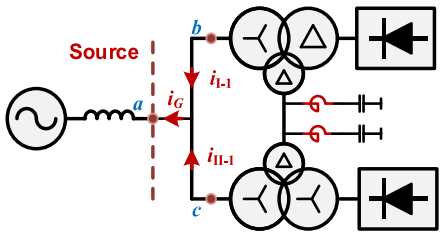

Fig. 11. Test point of prototype.

power test. The experimental wiring scheme is exhibited in Fig. 11, where 3 test points (*a*, *b*, and *c*) are chosen. Moreover, the connection of IFT-IR with filter and rectifier can be referred to Fig. 3.

A. Experiment 1: Transformer Test

IFT-IR is produced according to the parameters listed in the last line of Table I. From Table III, it can be found that the equivalent impedance of filtering winding is deviated from the absolute zero-impedance design. Fig. 12 shows the measured dimension of the prototype and its comparison with conventional IFT (without IR). The total area of IFT-IR with approximative zero-impedance design is 0.3 m^2, while the installation area of the conventional one is about 0.4 m^2. It can be calculated that 25% installation area is saved.

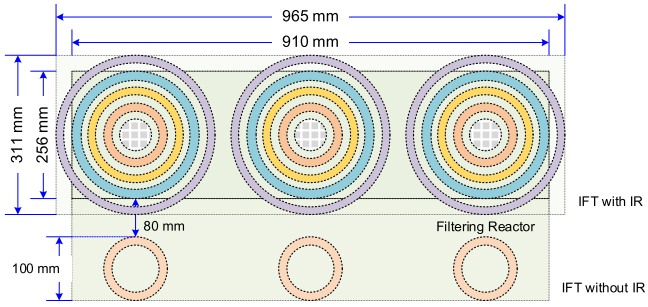

Fig. 12. Comparison of the installation space between the proposal and conventional IFT.

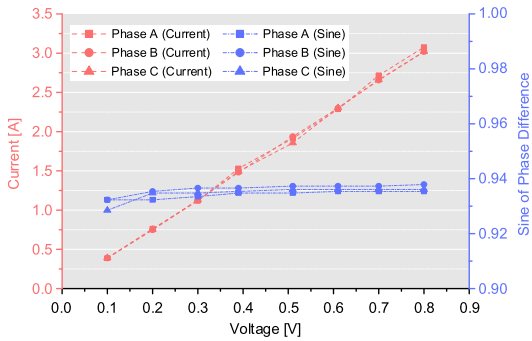

Fig. 13. Volt-ampere characteristics of IR.

Compared with the absolute zero-impedance design in Table I, the radial dimension of the prototype is further reduced by 3.2%. The reduced area can be calculated to be 6.3%.

Moreover, the volt-ampere test result of IR is shown in Fig. 13. Red line and blue line represent for the variation of current and sine of phase difference between voltage and current, respectively. The volt-ampere curve shows a good linearity. After computation, the inductance of IR is around 0.8 mH, and the error is less than 5%.

B. Experiment 2: Filtering Performance Test

Fig. 14 shows the test results of the proposed TIFM-SPSS, and Fig. 15 is the comparison test with the conventional structure (i.e., the parallel filtering winding and the filters are in open circuit). Table V lists the harmonic content. It can be observed from Fig. 14 that, with the help of the common bus and the shared filter, the currents induced at the primary side of the two transformers are with good quality, which validates the mathematical derivation in Section III. Power quality at *Point a* is considerably improved compared with conventional structure in Fig. 15.

It is worth noting the *highlighted part in red* in Table V that, all the $n = 6i \pm 1$ ($i = 1, 3, 5 \ldots$) order harmonic currents are inevitably induced at the primary side of the transformer in conventional structure (*Points b* and *c*). However, such phenomenon is not existed in the proposal, which means that these harmonics are offset each other in the common bus. It is considered as the main difference and innovation of the proposal. Total harmonic distortion (THD) of current at primary side (*Points b* and *c*) is greatly reduced, while the drop at source side reaches 34.7%.

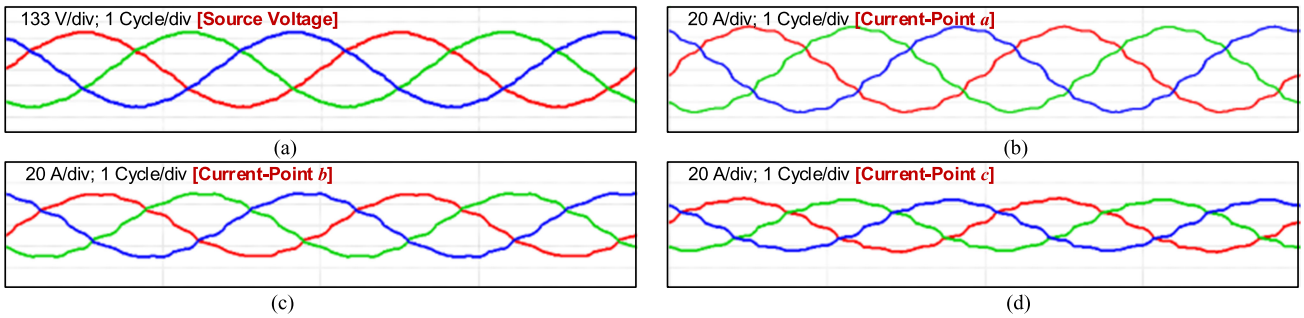

Fig. 14. Waveforms of primary side voltage and current for the proposal (recorded by HIOKI-PW 3198). (a) Source voltage. (b) Current at *Point a*. (c) Current at *Point b*. (d) Current at *Point c*.

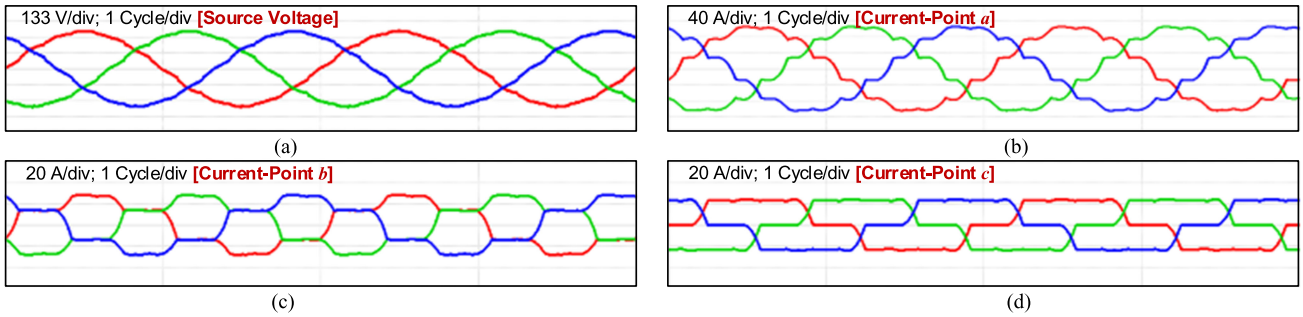

Fig. 15. Waveforms of primary side voltage and current for the conventional SPSS (recorded by HIOKI-PW 3198). (a) Source voltage. (b) Current at *Point a*. (c) Current at *Point b*. (d) Current at *Point c*.

TABLE V
HARMONIC CURRENT CONTENTS OF TEST RESULTS

Unit: [A]	Conventional Structure			Proposal		
Test Point	*a*	*b*	*c*	*a*	*b*	*c*
Fun.	36.72	18.57	18.17	36.93	18.67	18.32
3	0.03	0.02	0.04	0.03	0.01	0.02
5	0.32	3.53	3.25	0.34	0.31	0.34
7	0.49	2.19	2.35	0.60	0.40	0.22
11	2.49	1.26	1.25	1.37	0.59	0.79
13	1.42	0.69	0.75	1.08	0.53	0.55
17	0.16	0.39	0.40	0.16	0.08	0.08
19	0.13	0.28	0.29	0.11	0.06	0.05
23	0.39	0.22	0.17	0.34	0.16	0.18
25	0.27	0.13	0.15	0.28	0.13	0.14
THD [%]	8.11	23.23	23.08	5.29	4.73	6.24

Furthermore, the voltage harmonic spectrum is provided in Fig. 16, corresponding to Figs. 14(a) and 15(a). Most obviously, the content of 11th and 13th harmonics is reduced. However, this drop is not as sharp as the current harmonic, due to the impact of background harmonic. For the two scenarios, THD of voltage (THD_V) are 2.12% for TIFM-SPSS and 2.80% for traditional SPSS.

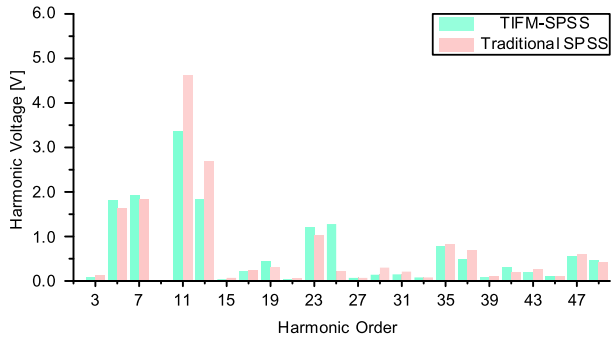

Fig. 16. Harmonic histogram of voltage at primary side of transformer.

C. Experiment 3: Fundamental Power Test

Table VI shows the test results of transformer efficiency. P_x ($x = 1$, 2 or 3) is the active power measured at the primary winding, load winding, and filtering winding (corresponding to W1, W2, and W3). η ($= P_2/P_1$) is the transformer efficiency. Second line of Table VI is the no-load loss of the transformer. Compared with the transformer efficiency before and after implementing filter, it can be found that the operating loss is reduced, while the efficiency of the whole supply system is increased by 0.87%, which can be attributed to the harmonic elimination and reactive power compensation at the secondary side. Moreover, P_3 in the Table indicates the low resistive loss in the filtering branches.

Furthermore, Table VII lists the test results of power factor of the conventional supply system (no filter) and the proposal. Compared with the conventional supply system, the reactive power in TIFM-SPSS is compensated due to the implementation of passive filter, which results in a high power factor.

TABLE VI
EFFICIENCY TEST RESULTS

Mode	Item	#1 (YDD)	#2 (YYD)	TIFM-SPSS
No load	P_1	0.085 kW	0.086 kw	0.171 kW
No filter	P_1	12.10 kW	11.90 kW	24.00 kW
	P_2	11.73 kW	11.55 kW	23.28 kW
	η (=P_2/P_1)	96.94%	97.06%	97.00%
With Filter	P_1	12.33 kW	12.14 kW	24.47 kW
	P_2	12.06 kW	11.89 kW	23.95 kW
	P_3	0.004 kW	0.004 kW	-
	η (=P_2/P_1)	97.81%	97.94%	97.87%

TABLE VII
POWER FACTOR TEST RESULTS

Mode	*Point a*	*Point b*	*Point c*
No load	0.9572	09572	0.9571
With filter	0.9957	-0.9830	0.9750

VI. CONCLUSION

A transformer integrated filtering method based shipboard power supply system, using IFT-IR as the core device, is proposed in this article. The proposal realizes the high integration of propulsion transformer and power filter, while it provides the harmonic-free power supply environment, which is beneficial to the stable operation and integrated optimization of the compact-design oriented all-electric shipboard. The noteworthy contributions of performance improvement include 25% reduction of installation space, 34.7% drop of current THD and 0.87% efficiency improvement.

The main theoretical findings are summarized as follows.

1) The filtering mechanism is explored, and the special harmonic path is revealed, which shows that most of the harmonics are cancelled out by the filtering bus bar and passive filter.
2) By means of the definition of approximative zero-impedance, the transformer size can be further optimized, the radial dimension can be theoretically reduced by as much as 9.21%.
3) The inductance calculation method of integrated reactor is analyzed. By adjusting the structural parameters, the distribution range of the inductance is obtained.

APPENDIX

Fig. A.1 shows the equivalent circuit model of TIFM-SPSS. According to basic circuit principle, ampere turns balance, and voltage relationship on the transformer, the following equations are obtained:

$$\begin{cases} N_1 i_{\#1-1} + N_2 i_{\#1-2} + N_3 i_{\#1-3} = 0 \\ N_1 i_{\#2-1} + \sqrt{3} N_2 i_{\#2-2} + N_3 i_{\#2-3} = 0 \end{cases} \tag{A.1}$$

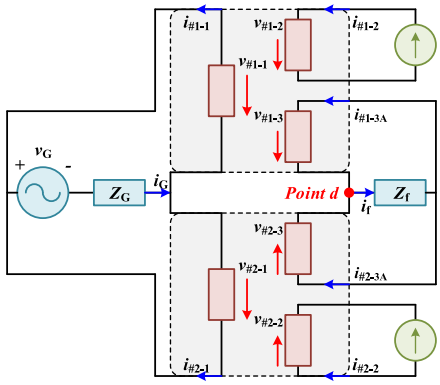

Fig. A.1. Single phase equivalent circuit model.

$$\begin{cases} v_{\#1-1} - \frac{N_1}{N_3} v_{\#1-3} = Z_{\#1-1} \cdot i_{\#1-1} - \frac{N_1}{N_3} Z_{\#1-3} \cdot i_{\#1-3} \\ v_{\#2-1} - \frac{N_1}{N_3} v_{\#2-3} = Z_{\#2-1} \cdot i_{\#2-1} - \frac{N_1}{N_3} Z_{\#2-3} \cdot i_{\#2-3} \end{cases} \tag{A.2}$$

$$v_{\#1-1} = v_{\#2-1} = v_G - Z_G \cdot i_G \tag{A.3}$$

where $i_{\#1\text{-k}}$ and $i_{\#2\text{-k}}$ (k = 1, 2, or 3) are the current flowing through the winding of two transformers; $Z_{\#1\text{-k}}$ and $Z_{\#2\text{-k}}$ are the equivalent impedance of transformer winding; to balance the load currents from two sides, $Z_{\#1\text{-k}}$ should be equal to $Z_{\#2\text{-k}}$ (i.e., $Z_{\#1\text{-k}} = Z_{\#2\text{-k}} = Z_k$); Z_f and Z_G are filter impedance and line impedance, respectively. Supposing that the generators have the ability of high-quality power supply, $v_G = 0$ for harmonic frequency.

For harmonic order $n = 12i \pm 1$, $(i = 1, 2, 3 \ldots)$, these harmonic currents will partly flow into the filters. The currents in two filter windings are expressed as

$$\begin{cases} i_{\#1-3} = \frac{cd-ab}{b^2-d^2} i_{\#1-2} + \frac{ad-bc}{b^2-d^2} i_{\#2-2} \\ i_{\#2-3} = \frac{ad-bc}{b^2-d^2} i_{\#1-2} + \frac{cd-ab}{b^2-d^2} i_{\#2-2} \end{cases} \tag{A.4}$$

where a, b, c, and d are referred to that

$$\begin{cases} a = \frac{N_2}{N_1} Z_1 + \frac{N_2}{N_1} Z_G \\ b = \frac{N_3}{N_1} Z_1 + \frac{N_3}{N_1} Z_G + \frac{N_1}{N_3} Z_3 + \frac{N_1}{N_3} Z_f \\ c = \frac{N_2}{N_1} Z_G \\ d = \frac{N_3}{N_1} Z_G + \frac{N_1}{N_3} Z_f. \end{cases} \tag{A.5}$$

After the confluence of currents into filters, the filter current can be obtained by

$$i_f = -\frac{a+c}{b+d}(i_{\#1-2} + i_{\#2-2}). \tag{A.6}$$

For tuned orders $n = 11$ and 13, $Z_f = 0$; for implementing inductive filtering method [22], $Z_3 = 0$; (A.6) is further simplified as

$$i_f = -\frac{N_2}{N_3}(i_{\#1-2} + i_{\#2-2}). \tag{A.7}$$

Equations (A.7) shows that all the tuned order harmonic currents from two load sides flow into the filters.

For harmonic order $n = 6i\pm1$ ($i = 1, 3, 5\ldots$), these harmonic currents are cancelled each other out at *Point d* (will not flow into filters) due to the 30° phase difference of two load windings. Hence, filter impedance can be regarded as infinite. Equations (A.8) shows that *all* the harmonic currents that order $n = 6i\pm1$ ($i = 1, 3, 5\ldots$) from two load sides are converged at *Point d*

$$i_{\#1-3} + i_{\#2-3} = -\frac{N_2}{N_3}(i_{\#1-2} + i_{\#2-2}). \tag{A.8}$$

In sum, the current transform ratio k_n from load side to filter side can be obtained

$$\begin{cases} k_n = -\frac{N_2}{N_3}, n = 11 \text{ or } 13 \\ k_n = -\frac{N_2}{N_3}, n = 6i \pm 1 (i = 1, 3, 5\ldots) \\ k_n = -\frac{a+c}{b+d}, n = \text{other}. \end{cases} \tag{A.9}$$

Moreover, the generator side current i_{G} is expressed as

$$i_G = \underbrace{\frac{\frac{2N_1N_2}{N_3^2}Z_{\mathrm{f}} + \frac{N_1N_2}{N_3^2}Z_3}{2Z_{\mathrm{G}} + Z_1 + \frac{2N_1^2}{N_3^2}Z_{\mathrm{f}} + \frac{N_1^2}{N_3^2}Z_3}}_{k_{\mathrm{G}n}}(i_{\#1-2} + i_{\#2-2}) \tag{A.10}$$

where $k_{\mathrm{G}n}$ (n is positive integer, and $n{\neq}6i\pm1$, $i = 1, 2, 3, 5, 7\ldots$) is the current transform ratio from load side to generator side.

REFERENCES

[1] A. Vicenzutti, R. Menis, and G. Sulligoi, "All-electric ship-integrated power systems: Dependable design based on fault tree analysis and dynamic modeling," *IEEE Trans Transport. Electrific.*, vol. 5, no. 3, pp. 812–827, Sep. 2019.

[2] Z. Jin, G. Sulligoi, R. Cuzner, L. Meng, J. C. Vasquez, and J. M. Guerrero, "Next-generation shipboard DC power system: Introduction smart grid and dc microgrid technologies into maritime electrical networks," *IEEE Electrific. Mag.*, vol. 4, no. 2, pp. 45–57, Jun. 2016.

[3] G. Sulligoi, A. Tessarolo, V. Benucci, A. Millerani Trapani, M. Baret, and F. Luise, "Shipboard power generation: Design and development of a medium-voltage dc generation system," *IEEE Ind. Appl. Mag.*, vol. 19, no. 4, pp. 47–55, Jul./Aug. 2013.

[4] T. Ericsen, N. Hingorani, and Y. Khersonsky, "Power electronics and future marine electrical systems," *IEEE Trans. Ind. Appl.*, vol. 42, no. 1, pp. 155–163, Jan./Feb. 2006.

[5] T. Hoevenaars, I. C. Evans, and A. Lawson, "New marine harmonic standards," *IEEE Ind. Appl. Mag.*, vol. 16, no. 1, pp. 16–25, Jan./Feb. 2010.

[6] W. Liu *et al.*, "Power quality assessment in shipboard microgrids under unbalanced and harmonic AC bus voltage," *IEEE Trans. Ind. Appl.*, vol. 55, no. 1, pp. 765–775, Jan./Feb. 2019.

[7] *IEEE Recommended Practice for Electrical Installations on Shipboard-Design*, IEEE Std 45.1-2017, 2017.

[8] *IEEE Recommended Practice for Establishing Transformer Capability When Supplying Nonsinusoidal Load Currents*, IEEE Stand C57.110-1998, 1998.

[9] J. Wimmer, M. R. R. Tanner, T. Nunn, and J. Kern, "Dry-type transformers: Specification, installation, and operational impacts in a marine environment," *IEEE Ind. Appl. Mag.*, vol. 19, no. 5, pp. 68–75, Sep./Oct. 2013.

[10] B. J. McRee, D. A. Wetz, D. A. Dodson, and J. M. Heinzel, "Hardware-in-the-Loop model validation of charging capacitors with multipulse rectifiers for high rep-rate shipboard-pulsed DC loads," *IEEE Trans. Plasma Sci.*, vol. 46, no. 10, pp. 3591–3598, Oct. 2018.

[11] Y. Terriche *et al.*, "A hybrid compensator configuration for VAR control and harmonic suppression in all-electric shipboard power systems," *IEEE Trans. Power Del.*, vol. 35, no. 3, pp. 1379–1389, Jun. 2020.

[12] E. Skjong, J. A. Suul, A. Rygg, T. A. Johansen, and M. Molinas, "System-wide harmonic mitigation in a diesel-electric ship by model predictive control," *IEEE Trans. Ind. Electron.*, vol. 63, no. 7, pp. 4008–4019, Jul. 2016.

[13] S. V. Giannoutsos and S. N. Manias, "A systematic power-quality assessment and harmonic filter design methodology for variable-frequency drive application in marine vessels," *IEEE Trans. Ind. Appl.*, vol. 51, no. 2, pp. 1909–1919, Mar./Apr. 2015.

[14] J. Kim and J. Lai, "Analysis of a shunt wye–delta transformer for multi-generator harmonic elimination under non-ideal phase-shift conditions," *IEEE Trans. Ind. Appl.*, vol. 55, no. 3, pp. 2412–2420, May/Jun. 2019.

[15] F. Meng, Q. Du, L. Wang, L. Gao, and Z. Man, "A series-connected 24-pulse rectifier using passive voltage harmonic injection method at DC-link," *IEEE Trans. Power Electron.*, vol. 34, no. 9, pp. 8503–8512, Sep. 2019.

[16] T. Wang, F. Fang, X. Jiang, K. Wang, and L. Yang, "Performance and design analysis on round-shaped transformers applied in rectifier systems," *IEEE Trans. Ind. Electron.*, vol. 64, no. 2, pp. 948–955, Feb. 2017.

[17] K. Nishizawa, J. Itoh, and A. Odaka, "Current harmonic reduction based on space vector PWM for DC-link capacitors in three-phase VSIs operating over a wide range of power factor," *IEEE Trans. Power Electron.*, vol. 34, no. 5, pp. 4853–4867, May 2019.

[18] J. Pan, Y. Yang, J. Li, F. Wang, Y. Abdullah, and L. Xu, "Control of high-performance drive feeding by four-level hybrid clamped converter for transportation electrification," *IEEE Trans Transport. Electrific.*, vol. 6, no. 2, pp. 568–577, Jun. 2020.

[19] J. Dai, S. W. Nam, M. Pande, and G. Esmaeili, "Medium-voltage current-source converter drives for marine propulsion system using a dual-winding synchronous machine," *IEEE Trans. Ind. Appl.*, vol. 50, no. 6, pp. 3971–3976, Nov./Dec. 2014.

[20] C. Liang *et al.*, "An integrated harmonic-filtering transformer for low-voltage distribution systems," *IEEE Trans. Magn.*, vol. 51, no. 11, Nov. 2006, Art. ID 8402204.

[21] *IEEE Standard for Requirements, Terminology, and Test Code for Dry-Type Air-Core Series-Connected Reactors*, IEEE Std C57.16-2011 (Revision of IEEE Std C57.16-1996), 2012.

[22] Y. Tian, L. Luo, Q. Liu, Y. Li, and Z. Huang, "A new harmonic mitigation system with double balanced impedance filtering power transformer for multistage distribution network," *IEEE Trans. Ind. Electron.*, vol. 68, no. 6, pp. 4565–4575, Jun. 2021.

[23] S. Kim, S. Kim, and D. Dujic, "Extending protection selectivity in DC shipboard power systems by means of additional bus capacitance," *IEEE Trans. Ind. Electron.*, vol. 67, no. 5, pp. 3673–3683, May 2020.

[24] F. L. Quilumba, R. E. Jimerson, K. Swift, and R. Garcia, "Positive- and zero-sequence impedance estimation of YNyn0+d-connected main power transformers in wind power applications," *CSEE J. Power Energy Syst.*, vol. 7, no. 1, pp. 57–65, Jan. 2021.

Qianyi Liu (Member, IEEE) was born in Sichuan, China, in 1992. He received the B.Sc. degree in electrical engineering and its automation (Railway Electrification) from the Department of Electrical Engineering, Southwest Jiaotong University, Chengdu, China, in 2014, and the M.Eng. and Ph.D. degrees in electrical engineering from the College of Electrical and Information Engineering, Hunan University, Changsha, China, in 2017 and 2020, respectively.

From 2019 to 2020, he was a Visiting Ph.D. Student at the Institute of Energy Systems, Energy Efficiency, and Energy Economics (ie^3), TU Dortmund University, Dortmund, Germany. Since 2021, he has been a Lecturer of Electrical Engineering with the School of Automation, Central South University, Changsha, China. His research interests include electric power optimization and control.

Fang Liu (Member, IEEE) was born in Jiangxi, China, in 1982. She received the B.S. degree from the College of Electric and Information Engineering, Zhengzhou University of Light Industry, Zhengzhou, China, in 2005, and the Ph.D. degree from Waseda University, Tokyo, Japan, in 2011.

She is a Professor with the School of Automation, Central South University, Changsha, China, since 2017. Her main research interests include stability analysis of time-delay system and power system, and robust control of FACTS with wide-area signals.

Runmin Zou received the B.Eng. degree in automatic control and the M.Eng. degree in control theory and control engineering from the Central South University (CSU), Changsha, China, in 1994 and 1997, respectively, and the Ph.D. degree in automatic control from the Ecole Centrale de Nantes, Nantes, France, in 2009.

Since 1997, he has been with the School of Automation, CSU, where he is currently a Full Professor. His main research interests include the intersection of control theory, artificial intelligence and power electronics with their applications to renewable energy, and complex dynamical systems.

Shaoyang Wang (Student Member, IEEE) was born in Hebei, China, in 1994. He received the B.Sc. and M.Eng. degrees from the College of Electrical and Information Engineering, Hunan University, Changsha, China, in 2017 and 2019, respectively. He is currently working toward the Ph.D. degree with the College of Electrical and Information Engineering, Hunan University, Changsha, China.

His research interests include power quality analyses and control.

Ye Tian was born in Zhuzhou, China, in 1994. He received the B.Sc. degree in automation from the Changsha University of Science and Technology, Changsha, China, in 2016, and the M.Sc. degree in electrical engineering from Hunan University, Changsha, China, in 2019. He is currently working toward the Ph.D. degree with the College of Electrical and Information Engineering, Hunan University, Changsha, China.

His research interests include power quality and control.

Yun Wang received the B.S. degree from Anhui University, Hefei, China, in 2012, the M.S. degree from the Lanzhou University, Lanzhou, China, in 2015, and the Ph.D. degree form Tianjin University, Tianjin, China, in 2019.

He is currently an Associate Professor with the School of Automation, Central South University, Changsha, China. His research interests include wind energy forecasting, big data analysis in power systems, robust regression modeling, multikernel learning, functional data analysis, Bayesian inference, and machine learning with uncertainty.

Liang Yuan received the B.Eng. degree from the Nanjing University of Science and Technology, Nanjing, China, in 2016, and the Ph.D. degree from the University of New South Wales, Kensington, Australia, in 2020.

He is currently with the School of Automation, Central South University. His research interests include integrated energy system and stability assessment of power systems with high penetration of renewables and power electronics.

Yong Li (Senior Member, IEEE) was born in Henan, China, in 1982. He received the B.Sc. and Ph.D. degrees from the College of Electrical and Information Engineering, Hunan University, Changsha, China, in 2004 and 2011, respectively, and the second Ph.D. degree from the Institute of Energy Systems, Energy Efficiency, and Energy Economics (ie^3), TU Dortmund University, Dortmund, Germany, in 2012.

Since 2009, he has been a Research Associate with the Institute of Energy Systems, Energy Efficiency, and Energy Economics (ie^3), TU Dortmund University, Dortmund, Germany. After then, he was a Research Fellow with The University of Queensland, Brisbane, Australia. Since 2014, he has been a Full Professor of electrical engineering with Hunan University. His current research interests include power system stability analysis and control, ac/dc energy conversion systems and equipment, analysis and control of power quality, and HVdc and FACTS technologies.